Coupling-Reduced Optimal Placement of Piezoelectric Actuators for Spacecraft with Flexible Telescope

GUO Yanning[1,2], *DENG Yuchen*[1], *RAN Guangtao*[1*], *LIU Fucheng*[3]

1. School of Astronautics, Harbin Institute of Technology, Harbin 150001, P. R. China; 2. Zhengzhou Research Institute, Harbin Institute of Technology, Zhengzhou 450000, P. R. China; 3. School of Aeronautics and Astronautics, Shanghai Jiao Tong University, Shanghai 200240, P. R. China

(Received 29 August 2025; revised 30 October 2025; accepted 30 November 2025)

Abstract: The oscillation of large space structure (LSS) can be easily induced because of its low vibration frequency. The coupling effect between LSS vibration control and attitude control can significantly reduce the overall performance of the control system, especially when the scale of flexible structure increases. This paper proposes an optimal placement method of piezoelectric stack actuators (PSAs) network which reduces the coupling effect between attitude and vibration control system. First, a spacecraft with a honeycomb-shaped telescope is designed for a resolution-critical imaging scenario. The coupling dynamics of the spacecraft is established using finite element method (FEM) and floating frame of reference formulation (FFRF). Second, a coupling-effect-reducing optimal placement criterion for PSAs based on coupling-matrix enhanced Gramian is designed to reduce the coupling effect excitation while balancing controllability. Additionally, a laddered multi-layered optimizing scheme is established to increase the speed and accuracy when solving the gigantic discrete optimization problem. Finally, the effectiveness of the proposed method is illustrated through numerical simulation.

Key words: large space structure (LSS); flexible spacecraft control; optimal placement of actuator; vibration control; rigid-flexible coupling spacecraft

CLC number: V448.2 **Document code:** A **Article ID:** 1005-1120(2025)06-0693-17

0 Introduction

Spacecraft with large space structure is increasingly attractive thanks to their broad mission potential. Recent advances in launching capability, deployable mechanisms[1], in-space assembly[2], 3D printing, are making the application practical. As the size of flexible appendages grows, such as solar panels, antennas[3], robot manipulators[4], on-orbit service devices[5], their low natural frequencies make vibration readily excited by disturbances like thermal environmental perturbations[6], space debris impact[7], on-orbit service operations[8], actuator faults[9], or maneuvering inputs.

Flexible spacecraft control strategies can be categorized into two types: Attitude control system (ACS) only, and attitude control with an active vibration control system (AVCS). Within ACS-only methods, passive control[10], e.g., input shaping[11], component synthesis[12], may work for spacecraft with small solar panels, but are sensitive to model uncertainties. Adaptive and robust techniques, e.g., parameter-adaptive fuzzy control[13], observer-based control[14-15], treat the coupling effect of the vibration of flexible appendages as disturbance. Passive stability can be guaranteed[16] when the flexible coupling matrix is small compared to the original inertia matrix of the spacecraft. For missions that strictly require precise pointing or structure shape, an AVCS is typically indispensable. Two frequently

---

*Corresponding author, E-mail address: ranguangtao@hit.edu.cn.

How to cite this article: GUO Yanning, DENG Yuchen, RAN Guangtao, et al. Coupling-reduced optimal placement of piezoelectric actuators for spacecraft with flexible telescope[J]. Transactions of Nanjing University of Aeronautics and Astronautics, 2025,42(6):693-709.

http://dx.doi.org/10.16356/j.1005-1120.2025.06.001

used AVCS approaches are independent modal space control (IMSC) and positive position feedback (PPF). They are often integrated with ACS, either as a combined strategy[17-18] or in a synergetic manner[19].

Actuator placement can significantly affect system performance in many ways. Efforts have been made to get better oscillation attenuation performance[20], maximum observability and controllability[21], minimum control effort[22-23], less spillover effect[24]. Analytical methods[25] are only feasible for simple structures like cantilevers. Heuristic optimization algorithms such as genetic algorithm (GA), particle swarm optimization (PSO), gray wolf[23] have been used for complex structures[26]. However, three gaps remain. First, most studies focus on small or moderate flexible structures[27] whose amount of truss varies from tens[28] to hundreds[29]. Optimal actuator placement of large space structure (LSS) which has up to thousands of trusses are seldom studied. Second, the existing criteria typically optimizes vibration suppression alone and ignores how placement influences attitude vibration coupling, which can degrade both attitude and vibration performance on LSS. Third, the increasing size and complexity of structure add challenges to modeling and solving of the optimization problem in an exponential way. Current optimization algorithms are prone to local convergence, which can render the outcomes infeasible.

In this study, an optimal vibration actuator placement strategy which reduces the coupling between ACS and AVCS for a spacecraft with a large space telescope structure is developed. The contributions of this paper can be listed as follows. (1) This paper proposes a model of a spacecraft operating in geostationary earth orbit (GEO). The model features a large, flexible, honeycomb-shaped telescope structure, which is inspired by typical LSS[1,30-31], and designed to meet high-resolution imaging requirements. (2) A coupling-matrix-enhanced Gramian is introduced, which weights vibrational modes based on their contributions to attitude-vibration coupling, thereby explicitly penalizing coupling effects while maintaining control lability. (3) A laddered multilayer GA featuring geometry-aware coding is developed to efficiently address the discrete optimization problem. This development facilitates the generation of a feasible layout for the network of piezoelectric stack actuators (PSAs).

This paper is organized as follows. Section 1 presents the development of the system model, encompassing the spacecraft geometry, the finite-element (FE) representation of the telescope, the model of the PSAs, and the coupled rigid-flexible dynamics. Section 2 formulates the actuator placement problem, introduces a geometry-aware coding approach, develops the coupling-reduced optimization criteria, and elaborates the laddered multi-layer GA solver. Simulation results are provided in Section 3 to show the effectiveness of the proposed method. Section 4 concludes the study.

1 Mathematical Model of Flexible Spacecraft

1.1 Geometric setup of the spacecraft

To facilitate the application of space telescope in high-resolution imaging scenarios, a honeycomb-shaped telescope with a large diameter is designed. Then, a spacecraft featuring a flexible telescope structure and a rigid hub is designed. As shown in Fig.1, according to the work in Ref.[31], the aperture of the telescope should reach up to 40 m to meet the angle resolution requirement of 10 mas for exoplanets observing.

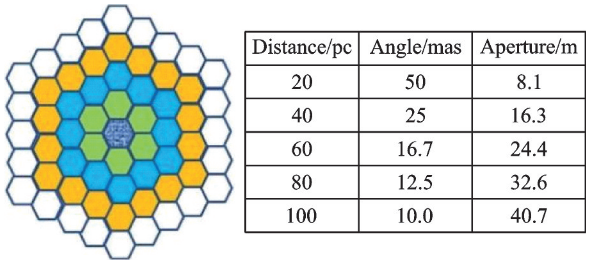

Distance/pc	Angle/mas	Aperture/m
20	50	8.1
40	25	16.3
60	16.7	24.4
80	12.5	32.6
100	10.0	40.7

Fig.1 Work in Ref.[31]

The space telescope structure is designed by our team as around 45 m of the diameter and is made up of more than 180 duplicated single hexagonal modules. Honeycomb structures are frequently used in large space structures, as shown in the recent research in Ref.[2]. It shows advantages in weight-reducing, thermal stability, mechanical rigidity, and small stowed volume for deployable mechanism. An array-style feed system, in which each individual module is equipped with its own feed source, enhances fault tolerance, improves precise beamforming and pointing, and increases the signal processing efficiency of the space telescope. The rigid hub where attitude actuators are installed, is connected to the central module of the telescope structure by rigid beams. A simplified beam-based model is established to facilitate the finite element method (FEM), optimal actuator placement and vibration control of the flexible spacecraft. The model is made up of 2 438 beams in total, and the material is supposed as carbon fiber (230 GPa), as is chosen in Ref.[32]. The side view, bottom view, and single module view of the spacecraft with deployed structure are shown in Fig.2. Twelve tip displacement probes are set on the edge of the structure to verify the vibration of the structure in Section 3, as marked as green diamonds in Fig.2. It is noteworthy that since the telescope structure is both axial and central symmetric, all modal shapes show axial or central symmetric patterns, which indicates that the energy transition also follows a symmetric pattern. The symmetric nature of modal shapes enlightens the development of the geometry-aware coding method, which is discussed in Section 2.3.

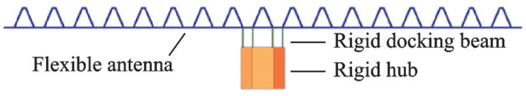

(a) Side view

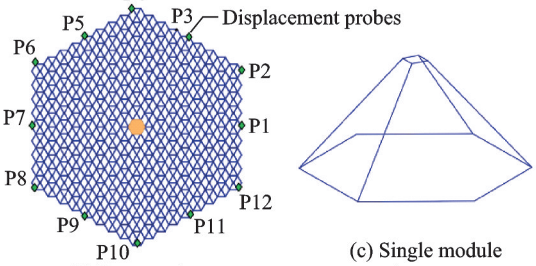

(b) Bottom view (c) Single module view

Fig.2 Geometric model of spacecraft

1.2 FEM model of the flexible telescope structure

The FEM model of the flexible structure is formulated in a beam-based way, that is, each single truss is modeled as two nodes and one element. Suppose the structure has n_0 nodes, each of which has three translational freedoms and three rotational freedoms, thus the total degree of freedom would be $n = 6n_0$. Let the number of installed actuators be n_a. And the dimension of disturbance force is n_d. The FEM model of the flexible structure is formulated as[33]

$$\boldsymbol{M}\ddot{\boldsymbol{\delta}}+\boldsymbol{C}\dot{\boldsymbol{\delta}}+\boldsymbol{K}\boldsymbol{\delta}=\boldsymbol{B}_{\mathrm{d}}\boldsymbol{f}_{\mathrm{d}}+\boldsymbol{B}_{\mathrm{a}}\boldsymbol{f}_{\mathrm{a}} \tag{1}$$

where $\boldsymbol{\delta}\in\mathbf{R}^{n\times 1}$ is the physical displacement of each degree of freedom of the nodes, $\boldsymbol{M}\in\mathbf{R}^{n\times n}$ the mass matrix, $\boldsymbol{C}\in\mathbf{R}^{n\times n}$ the damping matrix, and $\boldsymbol{K}\in\mathbf{R}^{n\times n}$ the stiffness matrix of the flexible structure; $\boldsymbol{f}_{\mathrm{d}}\in\mathbf{R}^{n_{\mathrm{d}}\times 1}$, $\boldsymbol{f}_{\mathrm{a}}\in\mathbf{R}^{n_{\mathrm{a}}\times 1}$ are the disturbance forces and the control forces, respectively, applied to the flexible appendages with respect to each degree of the mass elements of the system; $\boldsymbol{B}_{\mathrm{d}}\in\mathbf{R}^{n\times n_{\mathrm{d}}}$ and $\boldsymbol{B}_{\mathrm{a}}\in\mathbf{R}^{n\times n_{\mathrm{a}}}$ are the disturbance location matrix and the actuator installation matrix of the appendage, respectively. $\boldsymbol{M}$ and $\boldsymbol{K}$ are derived as follows. Each truss member of the honeycomb telescope is modeled as a straight Euler-Bernoulli beam element with two nodes and six degrees of freedom per node (three translations and three rotations). Let e denote a generic beam element with length L_e, cross-sectional area A, Young's modulus E, and density ρ . The local nodal displacement vector is

$$\boldsymbol{q}_e=\begin{bmatrix}\boldsymbol{q}_i\\ \boldsymbol{q}_j\end{bmatrix} \tag{2}$$

where

$$\boldsymbol{q}_i=[u_{xi}\quad u_{yi}\quad u_{zi}\quad \theta_{xi}\quad \theta_{yi}\quad \theta_{zi}]^{\mathrm{T}} \tag{3}$$

$$\boldsymbol{q}_j=[u_{xj}\quad u_{yj}\quad u_{zj}\quad \theta_{xj}\quad \theta_{yj}\quad \theta_{zj}]^{\mathrm{T}} \tag{4}$$

where subscripts i and j denote the two end nodes. Using standard beam shape functions, the displacement field along the element is interpolated from the nodal degrees of freedom as

$$\boldsymbol{\delta}_e(x)=\boldsymbol{N}_e(x)\boldsymbol{q}_e\qquad x\in[0,L_e] \tag{5}$$

$$\boldsymbol{\kappa}_e(x)=\boldsymbol{B}_e(x)\boldsymbol{q}_e\qquad x\in[0,L_e] \tag{6}$$

where $\boldsymbol{\delta}_e(x)$ collects the translational and rotational displacements of element e at the position x; $\boldsymbol{N}_e(x)$ the corresponding shape function matrix; $\boldsymbol{\kappa}_e(x)$ the bending curvature field; and $\boldsymbol{B}_e(x)$ the associated strain-displacement matrix for Euler-Bernoulli bending. The axial deformation is neglected since it contributes only to high frequency modes that lie far above the truncated modal bandwidth. The consistent element mass and stiffness matrices then follow the kinetic and strain energy as

$$M_e=\int_0^{L_e}\rho A\,\boldsymbol{N}_e^{\mathrm{T}}(x)\boldsymbol{N}_e(x)\,\mathrm{d}x \tag{7}$$

$$K_e=\int_0^{L_e}EI\,\boldsymbol{B}_e^{\mathrm{T}}(x)\boldsymbol{B}_e(x)\,\mathrm{d}x \tag{8}$$

where I is the second moment of area of the beam cross section. Let T_e be the Boolean transformation matrix that maps the local degrees of freedom $\boldsymbol{q}_e$ into the global physical displacement vector $\boldsymbol{\delta}\in\mathrm{R}^n$. The global mass and stiffness matrices in Eq.(1) are obtained by standard FE assembly over all $N_{\mathrm{b}}=2\,438$ beams

$$\boldsymbol{M}=\sum_{e=1}^{N_{\mathrm{b}}}\boldsymbol{T}_e^{\mathrm{T}}\boldsymbol{M}_e\boldsymbol{T}_e,\quad \boldsymbol{K}=\sum_{e=1}^{N_{\mathrm{b}}}\boldsymbol{T}_e^{\mathrm{T}}\boldsymbol{K}_e\boldsymbol{T}_e \tag{9}$$

Note that the present study is restricted to the small deformation linear regime in which modal decoupling is valid. The influence of nonlinear geometric coupling, thermal variations, or parameter-dependent modal changes is beyond the scope of this work and will be considered in future extensions.

1.3 Modal state-space model of the flexible telescope structure

According to the vibration theory, the physical displacement can be transformed into modal displacement as

$$\delta=\sum_{i=1}^{m}\boldsymbol{\Phi}_i\boldsymbol{\eta}_i=\boldsymbol{\Phi}\boldsymbol{\eta} \tag{10}$$

where $\boldsymbol{\Phi}\in\mathrm{R}^{n\times m}$ is the mode shape matrix; m the number of retained modes, and $\boldsymbol{\eta}\in\mathrm{R}^m$ the modal displacement vector considering m order mode. Substituting Eq.(10) into Eq.(1) yield

$$\boldsymbol{\Phi}^{\mathrm{T}}\boldsymbol{M}\boldsymbol{\Phi}\ddot{\boldsymbol{\eta}}+\boldsymbol{\Phi}^{\mathrm{T}}\boldsymbol{C}\boldsymbol{\Phi}\dot{\boldsymbol{\eta}}+\boldsymbol{\Phi}^{\mathrm{T}}\boldsymbol{K}\boldsymbol{\Phi}\boldsymbol{\eta}=\boldsymbol{\Phi}^{\mathrm{T}}\boldsymbol{B}_{\mathrm{d}}\boldsymbol{f}_{\mathrm{d}}+\boldsymbol{\Phi}^{\mathrm{T}}\boldsymbol{B}_{\mathrm{a}}\boldsymbol{f}_{\mathrm{a}} \tag{11}$$

Considering the normalized and orthogonal nature of mode shapes, $\boldsymbol{\Phi}^{\mathrm{T}}\boldsymbol{M}\boldsymbol{\Phi}=\boldsymbol{E}$. Let

$$\boldsymbol{C}_\eta=\boldsymbol{\Phi}^{\mathrm{T}}\boldsymbol{C}\boldsymbol{\Phi}=\mathrm{diag}[2\zeta_1\omega_1,2\zeta_2\omega_2,\cdots,2\zeta_m\omega_m] \tag{12}$$

$$\boldsymbol{K}_\eta=\boldsymbol{\Phi}^{\mathrm{T}}\boldsymbol{K}\boldsymbol{\Phi}=\mathrm{diag}[\omega_1^2,\omega_2^2,\cdots,\omega_m^2] \tag{13}$$

where ω_i is the vibration frequency of the ith mode; ζ_i the damping ratio of the ith mode. The first eight modal frequencies are illustrated in Table 1. The model adopting independent modal space control (IMSC) is obtained

$$\ddot{\boldsymbol{\eta}}+\boldsymbol{C}_\eta\dot{\boldsymbol{\eta}}+\boldsymbol{K}_\eta\boldsymbol{\eta}=\boldsymbol{u}+\boldsymbol{d} \tag{14}$$

where $\boldsymbol{u}$ is the modal control force; and $\boldsymbol{d}$ the modal disturbance force. Let $\boldsymbol{x}=[\boldsymbol{\eta}^{\mathrm{T}},\dot{\boldsymbol{\eta}}^{\mathrm{T}}]^{\mathrm{T}}$, and the system state-space expression can be written as

$$\boldsymbol{x}=\boldsymbol{A}\boldsymbol{x}+\boldsymbol{B}_{\mathrm{a}\boldsymbol{\Phi}}\boldsymbol{F}_{\mathrm{a}}+\boldsymbol{B}_{\mathrm{d}\boldsymbol{\Phi}}\boldsymbol{F}_{\mathrm{d}} \tag{15}$$

where A is a diagonal matrix made up of m matrices

$$\boldsymbol{A}_i=\begin{bmatrix}0 & 1\\ -\omega_i^2 & -2\zeta_i\omega_i\end{bmatrix} \tag{16}$$

where $A=\mathrm{blkdiag}(A_i)$, $i=[1, 2, \cdots, m]$. Elements in odd-numbered rows of $B_{\mathrm{a}\boldsymbol{\Phi}}\in\mathrm{R}^{2m\times m}$ all equals 0, while those in even numbered rows are made up of $\boldsymbol{\Phi}^{\mathrm{T}}B_{\mathrm{a}}$. $B_{\mathrm{d}\boldsymbol{\Phi}}$ is defined similarly as $\boldsymbol{B}_{\mathrm{a}\boldsymbol{\Phi}}$. $\boldsymbol{F}_{\mathrm{d}}$ is the disturbance force, and $\boldsymbol{F}_{\mathrm{a}}$ the control force produced by PSAs.

Table 1 Frequencies of first eight modes

Mode	Frequency/Hz	Mode	Frequency/Hz
1	0.102	5	0.335
2	0.109	6	0.366
3	0.133	7	0.457
4	0.291	8	0.501

To justify the modal truncation, we adopt a strain energy convergence criterion. For a linear elastic structure, the strain energy associated with mode i is

$$U_i=\frac{1}{2}\boldsymbol{\Phi}_i^{\mathrm{T}}\boldsymbol{K}\boldsymbol{\Phi}_i \tag{17}$$

Therefore, the cumulative strain energy ratio of the first m modes is

$$r_m^{\mathrm{SE}}=\frac{\sum_{i=1}^{m}\boldsymbol{\Phi}_i^{\mathrm{T}}\boldsymbol{K}\boldsymbol{\Phi}_i}{\sum_{i=1}^{N_m}\boldsymbol{\Phi}_i^{\mathrm{T}}\boldsymbol{K}\boldsymbol{\Phi}_i} \tag{18}$$

where N_m is the total number of computed modes. In the present model, $r_{10}^{\mathrm{SE}}>0.997$, which means that the retained ten constrained modes capture more than 99.73% of the total structural strain energy, and the truncated higher modes have negligible influence on the rigid-flexible coupling.

1.4 PSA installation and modeling

The minimum single module of the flexible honeycomb structure is used to explain the set up of the actuators (Fig.3). PSAs are frequently used in truss-based structures[34] to suppress the vibration. Due to the strict installation restrictions the deployable mechanism of structure applies on the structure, the offset stack type actuator which is considered in Ref.[35] is not chosen in this case. Besides, the pi-shaped configuration also needs to decide the direction angle along which the actuator is installed, which increases the complexity of the system design. The active vibration actuator considered in this paper is piezoelectric stack. The applicable placement locations of the actuators in a single module include two parts, all those six beams in the planar honeycomb structure and the four out-of-plane beams.

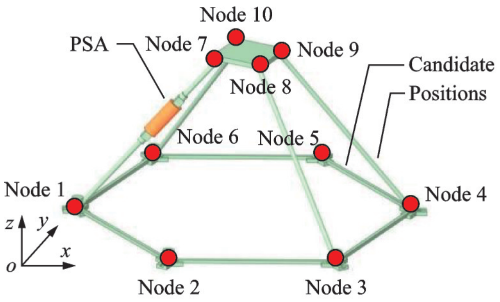

Fig.3 PSA installation

In Fig.3, ten nodes are included in each single module. The actuation force exerted by the piezoelectric stack is along the aligned line of the actuator. As mentioned F_a in Eq.(15), the position angle of the installed actuator respect to global coordinate are α, β, γ. The force applied to node 1 and node 7 would be $F_1 = -F_7$.

$$\begin{cases} F_1 = [\,F_a\cos\alpha \quad F_a\cos\beta \quad F_a\cos\gamma\,]^{\mathrm{T}} \\ F_7 = [\,-F_a\cos\alpha \quad -F_a\cos\beta \quad -F_a\cos\gamma\,]^{\mathrm{T}} \end{cases} \tag{19}$$

The installation matrix B_a of the actuator in the single module can be expressed as

$$B_a = \begin{bmatrix} [\,\cos\alpha \quad \cos\beta \quad \cos\gamma\,]^{\mathrm{T}} \\ 0_{5\times3} \\ [\,-\cos\alpha \quad -\cos\beta \quad -\cos\gamma\,]^{\mathrm{T}} \\ 0_{3\times3} \end{bmatrix}_{10\times3} \tag{20}$$

The electric-mechanical governing equation of a PSA can be expressed as[36]

$$f_a = \frac{Ac_{33}^{\mathrm{E}}}{nt}\boldsymbol{\delta}_{33} - \frac{Ad_{33}c_{33}^{\mathrm{E}}}{t}V \tag{21}$$

where A is the cross-sectional area of the stack; c_{33}^{E} the modulus under constant electric field in the stack axial direction; $\boldsymbol{\delta}_{33}$ the physical displacement of the stack; n the number of stack layers; t the thickness of each stack layer; d_{33} the piezoelectric constant of stack; and $V\in\mathbf{R}^{n_a\times1}$ the input voltage applied to the stack. Substituting Eq.(21) into Eq.(1) yields

$$\boldsymbol{M}\ddot{\boldsymbol{\delta}} + \boldsymbol{C}\dot{\boldsymbol{\delta}} + \tilde{\boldsymbol{K}}\boldsymbol{\delta} = \boldsymbol{B}_d f_d - \tilde{\boldsymbol{B}}_a V \tag{22}$$

where $\tilde{\boldsymbol{K}}$ and $\tilde{\boldsymbol{B}}_a$ are the modified stiffness matrix and the electro-mechanical installation matrix containing $\dfrac{Ad_{33}c_{33}^{E}}{nt}$ and $\dfrac{A}{nt}$, respectively. The modified modal space equation can be derived from Eq.(15) similarly as

$$\dot{\boldsymbol{x}} = \tilde{\boldsymbol{A}}\boldsymbol{x} + \tilde{\boldsymbol{B}}_{a\boldsymbol{\Phi}}\boldsymbol{F}_a + \boldsymbol{B}_{d\boldsymbol{\Phi}}\boldsymbol{F}_d \tag{23}$$

It is assumed here that changes to the mass and the stiffness matrices introduced by the PSA are negligible.

1.5 Dynamic model of flexible spacecraft

The flexible spacecraft dynamics derived from Eq.(14) and the rigid spacecraft dynamics[37] can be expressed as

$$\begin{cases} \hat{\boldsymbol{M}}_{\mathrm{flex}}\begin{bmatrix}\dot{\boldsymbol{v}} \\ \dot{\boldsymbol{\omega}}\end{bmatrix} - \begin{bmatrix}\sum\limits_{i=1}^{m}\boldsymbol{B}_{\mathrm{tran}-i}\ddot{\boldsymbol{\eta}} \\ \sum\limits_{i=1}^{m}\boldsymbol{B}_{\mathrm{rot}-i}\ddot{\boldsymbol{\eta}}\end{bmatrix} = \begin{bmatrix}\boldsymbol{F} \\ \boldsymbol{T}\end{bmatrix} \\ \ddot{\boldsymbol{\eta}} + 2\boldsymbol{\zeta}\boldsymbol{\omega}\dot{\boldsymbol{\eta}} + \boldsymbol{\omega}^2\boldsymbol{\eta} + \boldsymbol{B}_{\mathrm{rot}}^{\mathrm{T}}\dot{\boldsymbol{\omega}} + \boldsymbol{B}_{\mathrm{tran}}^{\mathrm{T}}\dot{\boldsymbol{v}} = \boldsymbol{u} + \boldsymbol{d} \end{cases} \tag{24}$$

where $\hat{\boldsymbol{M}}_{\mathrm{flex}}$ is the generalized inertia matrix of the flexible spacecraft; and F and T are the control force and the torque applied to mass center of spacecraft, respectively.

$$\hat{\boldsymbol{M}}_{\mathrm{flex}} = \begin{bmatrix}\boldsymbol{M}_{11} & \boldsymbol{M}_{12} \\ \boldsymbol{M}_{21} & \boldsymbol{M}_{22}\end{bmatrix} \tag{25}$$

$$\begin{cases} \boldsymbol{M}_{11} = m\boldsymbol{E}_3 - \boldsymbol{B}_{\mathrm{tran}}^{\mathrm{T}}\boldsymbol{B}_{\mathrm{tran}} \\ \boldsymbol{M}_{12} = -\boldsymbol{B}_{\mathrm{tran}}^{\mathrm{T}}\boldsymbol{B}_{\mathrm{rot}} \\ \boldsymbol{M}_{21} = -\boldsymbol{B}_{\mathrm{rot}}^{\mathrm{T}}\boldsymbol{B}_{\mathrm{tran}} \\ \boldsymbol{M}_{22} = \boldsymbol{I} - \boldsymbol{B}_{\mathrm{rot}}^{\mathrm{T}}\boldsymbol{B}_{\mathrm{rot}} \end{cases} \tag{26}$$

where $\boldsymbol{B}_{\mathrm{tran}}$, $\boldsymbol{B}_{\mathrm{rot}}\in\mathbf{R}^{3\times m}$ are the translational and the rotational coupling matrixes of the spacecrafts, respectively.

$$\begin{cases} B_{\text{tran}} = \sum_{k=1}^{n_a} \boldsymbol{m}_k \boldsymbol{\Phi}_k \\ B_{\text{rot}} = \sum_{k=1}^{n_a} \boldsymbol{m}_k (\tilde{\boldsymbol{l}} \boldsymbol{\Phi}_k + \boldsymbol{r}_k \boldsymbol{\Phi}_k) \end{cases} \tag{27}$$

where $k \in [1, 2, \cdots, n_0]$ denotes the kth node of the structure; $\boldsymbol{\Phi}_k \in \mathrm{R}^{3\times n}$ the mode shape matrix of the kth node; $\boldsymbol{m}_k \in \mathrm{R}^{3\times 1}$ the mass matrix of the kth node; $\boldsymbol{r}_k$ the position vector from the kth node to the origin of the telescope coordinate; and $\tilde{\boldsymbol{l}}$ the cross product matrix of $\boldsymbol{l}$, which is the vector from telescope coordinate origin to the spacecraft coordinate origin. Since the spacecraft considered in this work operates in GEO, the air drag disturbance is neglected. Meanwhile, due to the geometric symmetry of the spacecraft and the near coincidence between its geometric center and center of mass, the solar radiation torque is not considered.

2 Placement Optimization of PSA of Space Telescope

2.1 Optimization problem statement

Using the applicable placement locations discussed in Section 1.4, the number of possible combinations would be too large for the traversal method when multiple actuators are installed. Besides, the gigantic data storage space it takes would be up to several hundreds of millions TB. In this case, among all 2 438 beams of the antenna, the number of applicable positions is 1 570. If the number of actuators is 8, the number of possible combinations would be 8.9 × 1 020, and the data storage demand would be 8.18 × 108 TB, which is not tolerable in practical application.

Let the number of feasible locations be $n_{\mathrm{p}} \in \mathrm{N}$, the possible location set of actuators is $\{1, 2, \cdots, n_{\mathrm{p}}\}$. The number of actuators is n_{a}, $1 \leqslant n_{\mathrm{a}} \leqslant n_{\mathrm{p}}$. The sequence of actuator locations L is represented as $\{l_1, l_2, \cdots, l_i, \cdots, l_{n_{\mathrm{a}}}\}$, where l_i denotes the location of the ith actuator, $1 \leqslant l_i \leqslant n_{\mathrm{p}}$. Then the objective of the optimization is to determine L that achieves the best optimal criteria.

2.2 Multilayer geometry-aware coding for GA

Since the gigantic number of optional locations of the actuators, these positions should be coded in a sorted way for the benefit of initializing and searching efficiency of GA. A multi-layered coding scheme which maps the physical candidate positions P expressed as $\{l_1, l_2, \cdots, l_{n_{\mathrm{p}}}\}$ to an index-based position coding $[1, 2, \cdots, n_{\mathrm{p}}]$ is thus proposed to meet the requirement of gigantic searching space. As shown in Fig.4, the Cartesian coordinate of l_i is $(p_{i1}(x_{i1}, y_{i1}, z_{i1}), p_{i2}(x_{i2}, y_{i2}, z_{i2}))$, and whose midpoint in cylindrical coordinates is $p_i(\rho_i, \theta_i, z_i)$. A sorting priority criteria is designed to be multilayered based on geometric layout of optional locations, mathematically described by function of l_i, p_i.

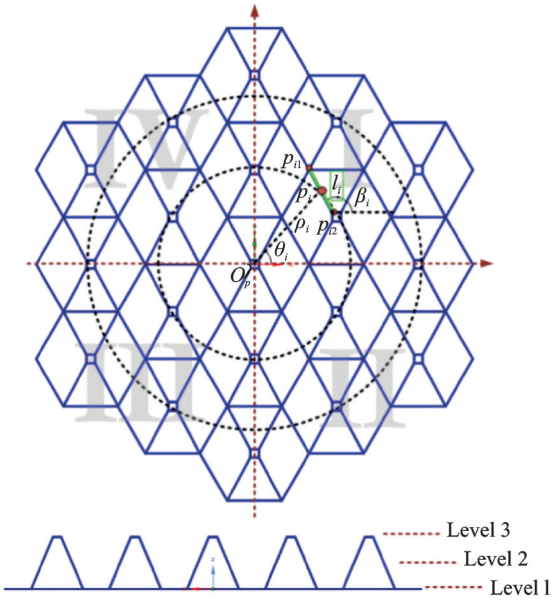

Fig.4 Geometry for coding

The first priority criteria is the quadrant of p_i (Ⅰ—Ⅱ—Ⅲ—Ⅳ). The second is the slope of the line connecting O_p and p_i, $\tan\theta_i$. The third is the displacement of p_i with respect to O_p, ρ_i. The fourth is the slope l_i, $\tan\beta_i = \dfrac{y_{i2} - y_{i1}}{x_{i2} - x_{i1}}$. The fifth is the planar level of l_i. The coding scheme is illustrated as in Table 2.

Table 2 Multi-layer coding scheme

Priority	Criteria	Ranging map
1	Quadrant	Ⅰ→Ⅱ→Ⅲ→Ⅳ
2	$\tan\theta_i$	$+\infty \to -\infty$
3	ρ_i	$0 \to \rho_{\max}$
4	$\tan\beta_i$	$+\infty \to -\infty$
5	Level	1→3

Remark 1 The coding sequence designed here not only benefits the search efficiency of the genetic algorithm, but also facilitates the successive initialization of the population, which will be discussed in Section 2.4

2.3 Coupling-reduced optimal criteria and constraints

A coupling-matrix enhanced Gramian-based optimal criteria inspired by Ref.[37] is proposed in this section to take the pose-vibrational coupling effect into account when optimizing the placement of PSAs. Based on the state-space model Eq.(23) presented in Section 1.4, suppose the initial state of the system is $\boldsymbol{x}_0$, the expected state at $t = T_\mathrm{f}$ is $\boldsymbol{x}_\mathrm{f}$, the control effort during this period is formulated as

$$J=\int_0^{T_\mathrm{f}} \boldsymbol{u}^\mathrm{T}(t)\boldsymbol{u}(t)\mathrm{d}t \tag{28}$$

According to Pontryagin's maximum principle, the control effort can also be denoted as

$$J=(\mathrm{e}^{\boldsymbol{A}T_\mathrm{f}}\boldsymbol{x}_0-\boldsymbol{x}_\mathrm{f})^\mathrm{T}\boldsymbol{W}_\mathrm{c}T_\mathrm{f}(\mathrm{e}^{\boldsymbol{A}T_\mathrm{f}}\boldsymbol{x}_0-\boldsymbol{x}_\mathrm{f}) \tag{29}$$

where $\boldsymbol{W}_\mathrm{c}T_\mathrm{f}$ is the Gramian controllability matrix that can be derived from Eq.(30), whose norm reflects the energy consumption

$$\boldsymbol{A}\boldsymbol{W}_\mathrm{c}T_\mathrm{f}+\boldsymbol{W}_\mathrm{c}T_\mathrm{f}\boldsymbol{A}^\mathrm{T}=\mathrm{e}^{\boldsymbol{A}T_\mathrm{f}}\boldsymbol{B}\boldsymbol{B}^\mathrm{T}\mathrm{e}^{\boldsymbol{A}^\mathrm{T}T_\mathrm{f}}-\boldsymbol{B}\boldsymbol{B}^\mathrm{T} \tag{30}$$

The controllability and energy consumption of the system can be optimized through the criteria[37] as

$$\mathrm{Crit}_\mathrm{A}=\frac{\mathrm{trace}(\boldsymbol{W}_\mathrm{c})\sqrt[2n_\mathrm{c}]{\det(\boldsymbol{W}_\mathrm{c})}}{\sigma(\lambda_j)} \tag{31}$$

Since reducing the non-negligible coupling effect between the flexible structure and the rigid hub is the main concern of the study, a new criteria is proposed to take the pose-vibration coupling effect into account, by weighting the Gramian controllability matrix according to the extent each mode contributes to the coupling matrix.

The total energy transferred to the structure from the actuators is defined as

$$\begin{aligned}\boldsymbol{E}=&\int_0^\infty(\boldsymbol{E}_\mathrm{p}(t)+\boldsymbol{E}_\mathrm{k}(t))\mathrm{d}t=\\&\frac{1}{2}\int_0^\infty\sum_{i=1}^m(\dot{\boldsymbol{\eta}}_i^2(t)+\boldsymbol{\eta}_i^2(t))\mathrm{d}t\end{aligned} \tag{32}$$

where $\boldsymbol{E}_\mathrm{p}$ and $\boldsymbol{E}_\mathrm{k}$ are the potential and the kinetic energy of vibration, respectively. From Eq.(23), neglecting the disturbance term, the system response under a dirac input $\boldsymbol{\delta}(t)$ would be

$$\boldsymbol{x}(t)=[\boldsymbol{\eta}(t),\dot{\boldsymbol{\eta}}(t)]=\mathrm{e}^{\tilde{A}t}\tilde{\boldsymbol{B}}_{\mathrm{a}\boldsymbol{\Phi}} \tag{33}$$

Since the Gramian controllability matrix can be calculated from Eq.(30) as

$$\boldsymbol{W}_\mathrm{c}T_\mathrm{f}=\int_0^{T_\mathrm{f}}\mathrm{e}^{\tilde{A}t}\tilde{\boldsymbol{B}}_{\mathrm{a}\boldsymbol{\Phi}}\tilde{\boldsymbol{B}}_{\mathrm{a}\boldsymbol{\Phi}}^\mathrm{T}\mathrm{e}^{\tilde{A}^\mathrm{T}t}\mathrm{d}t \tag{34}$$

It can be derived from Eqs.(32—34) that

$$\boldsymbol{E}=\frac{1}{2}\mathrm{trace}(\boldsymbol{W}_\mathrm{c})=\frac{1}{2}\sum_{i=1}^N(\boldsymbol{W}_{\mathrm{c}_{2i,2i}}+\boldsymbol{W}_{\mathrm{c}_{2i-1,2i-1}}) \tag{35}$$

From Eq.(24), the coupling attitude torque induced by vibration is

$$\boldsymbol{T}_\mathrm{flex}=\sum_{i=1}^m\boldsymbol{B}_{\mathrm{rot}\text{-}i}(2\zeta_i\omega_i\dot{\boldsymbol{\eta}}_i+\omega_i^2\boldsymbol{\eta}_i) \tag{36}$$

The energy transferred from the flexible structure to the attitude motion of rigid body through coupling effect can be expressed as

$$\begin{aligned}\boldsymbol{E}_\mathrm{c}=&\sum_{j=1}^3\int_0^\infty T_{\mathrm{flex}\text{-}j}\mathrm{d}t=\\&\sum_{j=1}^3\int_0^\infty\sum_{i=1}^m\boldsymbol{B}_\mathrm{rot}^\mathrm{T}(i,j)(2\xi_i\omega_i\dot{\boldsymbol{\eta}}_i(t)+\omega_i^2\boldsymbol{\eta}_i(t))\mathrm{d}t\end{aligned} \tag{37}$$

where $j=1, 2, 3$ denotes the three rotational axises. Eq.(37) can be further expressed as

$$\begin{aligned}\boldsymbol{E}_\mathrm{c}=&\sum_{j=1}^3\sum_{i=1}^m 2\xi_i\omega_i\int_0^\infty\boldsymbol{B}_\mathrm{rot}^\mathrm{T}(i,j)\left(\dot{\boldsymbol{\eta}}_i(t)+\frac{\omega_i}{2\xi_i}\boldsymbol{\eta}_i(t)\right)\mathrm{d}t=\\&\boldsymbol{A}_{\xi_i\omega_i}\mathrm{trace}(\boldsymbol{B}_{\mathrm{rot}\text{-}\mathrm{ext}}\sqrt{\boldsymbol{W}_\mathrm{c}})\end{aligned} \tag{38}$$

where $\boldsymbol{A}_{\xi_i\omega_i}$ is a constant matrix related to ξ_i and ω_i; $\sqrt{\boldsymbol{W}_\mathrm{c}}$ is calculated by the square root of each element of $\boldsymbol{W}_\mathrm{c}$, and $\boldsymbol{B}_{\mathrm{rot}\text{-}\mathrm{ext}}\in\mathbf{R}^{2m\times 2m}$ is a extended matrix of $\boldsymbol{B}_\mathrm{rot}$.

$$\begin{cases}\boldsymbol{B}_{\mathrm{rot}\text{-}\mathrm{ext}}=\mathrm{blkdiag}(s_1\boldsymbol{D}_1, s_2\boldsymbol{D}_2,\cdots, s_m\boldsymbol{D}_m)\\ \boldsymbol{D}_i=\begin{bmatrix}1 & 0\\ 0 & \dfrac{\omega_i}{2\xi_i}\end{bmatrix}\\ s_i\triangleq\displaystyle\sum_{j=1}^3\boldsymbol{B}_\mathrm{rot}(i,j)\quad i=1,2,\cdots,m\end{cases} \tag{39}$$

The optimization target is to maximize the energy $\boldsymbol{E}$ transferred from the actuator to the structure while balancing, if not minimizing the energy E_c transferred from the structure to the rigid body attitude. In other word, to maximize the actuator efficiency while reducing the coupling effect, it can be interpreted in Eq.(40) , considering Eq.(35) and Eq.(38).

$$T_{\mathrm{opt}}=\frac{\boldsymbol{E}}{\boldsymbol{E}_{\mathrm{c}}}=\frac{\operatorname{trace}(\boldsymbol{W}_{\mathrm{c}})}{2\operatorname{trace}(\boldsymbol{B}_{\text{rot-ext}}\sqrt{\boldsymbol{W}_{\mathrm{c}}})}=\frac{1}{2}\operatorname{trace}(\boldsymbol{B}_{\text{rot-ext}}^{-1}\sqrt{\boldsymbol{W}_{\mathrm{c}}}) \tag{40}$$

For simplicity of the optimization, T_{opt} is designed in a simpler form

$$T_{\mathrm{opt}}=\operatorname{trace}(\boldsymbol{P}_{\mathrm{diag}}\boldsymbol{W}_{\mathrm{c}}) \tag{41}$$

where the diagonal weight matrix $\boldsymbol{P}_{\mathrm{diag}}$ is defined as

$$\begin{cases}\boldsymbol{P}_{\mathrm{diag}}=\begin{bmatrix}\boldsymbol{P}_{\mathrm{diag}}(2i-1,2i-1) & 0\\ 0 & \boldsymbol{P}_{\mathrm{diag}}(2i,2i)\end{bmatrix}_{2n_{\mathrm{c}}\times 2n_{\mathrm{c}}}\\ \boldsymbol{P}_{\mathrm{diag}}(2i-1,2i-1)=\sum_{j=1}^{3}\boldsymbol{B}_{\mathrm{rot}}^{-1}(i,j)\\ \boldsymbol{P}_{\mathrm{diag}}(2i,2i)=\frac{2\xi_i}{\omega_i}\sum_{j=1}^{3}\boldsymbol{B}_{\mathrm{rot}}^{-1}(i,j)\end{cases} \tag{42}$$

where $i\in\{1,2,\cdots,n_{\mathrm{c}}\}$, $n_{\mathrm{c}}<m$ is the number of modes controlled in total m modes. Eq.(41) shows that the optimization target can be achieved through weighting $\boldsymbol{W}_{\mathrm{c}}$ by matrix $\boldsymbol{P}_{\mathrm{diag}}$, and the weighting factor is defined through checking the value distribution of rotational coupling matrix $\boldsymbol{B}_{\mathrm{rot}}$. $\boldsymbol{B}_{\mathrm{rot}}$ and $\boldsymbol{B}_{\mathrm{tran}}$ are illustrated in the appendix. It shows the main contributors to rotational x, y, z axses are modes 3, 1, 6, respectively. While for the translational movement, the coupling effect mainly takes place along z axis, affected by modes 2, 4.

Although the attitude stabilization is the main control objective for the telescope, the designed target Eq.(41) still has its functionality for translational coupling-effect damping due to the inner connection between $\boldsymbol{B}_{\mathrm{rot}}$ and $\boldsymbol{B}_{\mathrm{tran}}$, since by transforming Eq.(27), the $\boldsymbol{B}_{\mathrm{rot}}$ can be expressed in term of $\boldsymbol{B}_{\mathrm{tran}}$.

$$\boldsymbol{B}_{\mathrm{rot}}=\tilde{\boldsymbol{l}}\boldsymbol{B}_{\mathrm{tran}}+\sum_{k=1}^{n_0}\boldsymbol{m}_k\boldsymbol{r}_k\boldsymbol{\Phi}_k \tag{43}$$

It shows that the value of $\boldsymbol{B}_{\mathrm{rot}}$ also relies on $\boldsymbol{B}_{\mathrm{tran}}$, depending on $\tilde{\boldsymbol{l}}$. Eq.(43) shows the optimizing target considered in Eq.(41) has naturally considered the translational effect. To further enable the algorithm to adjust its attention to the translational coupling effect, $\boldsymbol{P}_{\mathrm{diag}}$ is modified as

$$\begin{cases}\tilde{\boldsymbol{P}}_{\mathrm{diag}}(2i-1,2i-1)=\boldsymbol{H}_{\mathrm{tran}}\sum_{j=1}^{3}\boldsymbol{B}_{\mathrm{tran}}^{-1}(i,j)+\\ \qquad\boldsymbol{H}_{\mathrm{rot}}\sum_{j=1}^{3}\boldsymbol{B}_{\mathrm{rot}}^{-1}(i,j)\\ \tilde{\boldsymbol{P}}_{\mathrm{diag}}(2i,2i)=\boldsymbol{H}_{\mathrm{tran}}\sum_{j=1}^{3}\boldsymbol{B}_{\mathrm{tran}}^{-1}(i,j)+\\ \qquad\boldsymbol{H}_{\mathrm{rot}}\frac{2\xi_i}{\omega_i}\sum_{j=1}^{3}\boldsymbol{B}_{\mathrm{rot}}^{-1}(i,j)\end{cases} \tag{44}$$

where

$$\begin{cases}\boldsymbol{H}_{\mathrm{tran}}=\|\boldsymbol{l}\|_2\\ \boldsymbol{H}_{\mathrm{rot}}=\frac{\sum\|\boldsymbol{r}_k\|_2}{k}+\|\boldsymbol{l}\|_2\end{cases} \tag{45}$$

where $\|\bullet\|_2$ is the norm 2 of a vector; and $\boldsymbol{r}_k$ and $\boldsymbol{l}$ are defined in Eq.(27). Note that in Eq.(44), the coefficient $\boldsymbol{H}_{\mathrm{tran}}$ and $\boldsymbol{H}_{\mathrm{rot}}$ smoothly regulate the balance between attitude-vibration coupling effect and orbit-vibration coupling effect reducing performance. The larger the average distance of structure nodes from the spacecraft center, the more attention will be paid to the attitude-vibration coupling effect, while the attitude-vibration coupling keeps its priority since $\frac{\boldsymbol{H}_{\mathrm{rot}}}{\boldsymbol{H}_{\mathrm{tran}}}\geqslant 1$ always holds. Now, the optimization target Eq.(41) can be modified as

$$\tilde{T}_{\mathrm{opt}}=\operatorname{trace}(\tilde{\boldsymbol{P}}_{\mathrm{diag}}\boldsymbol{W}_{\mathrm{c}}) \tag{46}$$

Then, inspired from the criteria in Eq.(31) , which uses $\sqrt[2n_{\mathrm{c}}]{\det(\boldsymbol{W}_{\mathrm{c}})}$ and $1/(\sigma(\lambda))$ to punish the results where poorly controllable mode exists, the following modified control Gramian matrix $\tilde{\boldsymbol{W}}_{\mathrm{c}}$ and criteria is designed. $\tilde{\boldsymbol{W}}_{\mathrm{c}}$ is defined as

$$\tilde{\boldsymbol{W}}_{\mathrm{c}}=\tilde{\boldsymbol{P}}_{\mathrm{diag}}\boldsymbol{W}_{\mathrm{c}}\tilde{\boldsymbol{P}}_{\mathrm{diag}}^{\mathrm{T}} \tag{47}$$

The criteria is designed as

$$\mathrm{Crit}_{\mathrm{B}}=\frac{\operatorname{trace}(\tilde{\boldsymbol{W}}_{\mathrm{c}})\sqrt[2n_{\mathrm{c}}]{\det(\tilde{\boldsymbol{W}}_{\mathrm{c}})}}{\sigma(\lambda_j)} \tag{48}$$

where $\sigma(\lambda_j)$ denotes the standard deviation of eigenvalue of $\tilde{\boldsymbol{W}}_{\mathrm{c}}$. The term $1/\sigma(\lambda_j)$ discourages actuator placements that lead to a highly ill-conditioned coupling-weighted controllability Gramian. A large $\sigma(\lambda_j)$ indicates a highly dispersed Gramian spectrum, meaning that some modal directions are much less controllable than others. Therefore, dividing by $\sigma(\lambda_j)$ penalizes such poorly balanced controllability, which helps avoid residual coupling dominated by weakly controllable modes.

As can be summarized, in the new designed criteria, the more influence a certain mode contributes to the coupling effect, the less weight the corresponding mode would have in the modified Gramian matrix. From former analysis, $\tilde{\boldsymbol{P}}_{\mathrm{diag}}$ is a diagonal weighting matrix reflecting the extent each mode of the flexible antenna contributes to the coupling effect. By doing so, the vibration caused by modals which are the main contributors of the coupling effect will be better controlled. Thus the excited coupling effect will be reduced, which leads to an improvement of the overall performance of both vibration and attitude control performance of the spacecraft.

As discussed in Section 1, the vibration modal shape of the large flexible antenna studied in this paper exhibits an axial or central symmetric pattern. The ideal layout of the piezoelectric stack actuators should be quasi-symmetric as well. This nature can be interpreted as constraints of the optimization process, by setting the quantity of actuators as four different quadrants identical. Additionally, to avoid the infeasible case where duplicated positions are included in solution L, the elements in L are constrained as strictly descending between the upper and lower bound of l_i. The constraints can be described as

$$\begin{cases} n_{q1}=n_{q2}=n_{q3}=n_{q4} \\ l_1>l_2>\cdots>l_i>\cdots>l_{n_{\mathrm{a}}-1}>l_{n_{\mathrm{a}}} \\ n\geqslant l_i\geqslant 1 \\ l_i\in \mathbf{Z} \end{cases} \tag{49}$$

Remark 2 The quadrant-based restriction is a rough yet effective way to utilize the symmetric nature of the vibration mode shape.

2.4 Laddered multilayer GA scheme

To speed up the convergence process and accuracy of the optimization problem, a successive optimization mechanism is designed. Suppose the anticipated number of actuators is $n_{\mathrm{a}}=4n$, the optimization process is disassembled into n loops. The initial population of each loop is a function of the outcome of its predecessor loop. Suppose the outcome of the first loop is

$$[l_{11}, l_{12}, l_{13}, l_{14}] \tag{50}$$

The original population $[l_{21}, l_{22}, \cdots, l_{2i}, \cdots, l_{28}]$ of the next loop is generated by interpolation, and $\lfloor x\rfloor$ denotes the floor function of variable x.

$$\left[\left\lfloor\frac{1+l_{11}}{2}\right\rfloor,\quad l_{11},\quad \left\lfloor\frac{1+l_{12}}{2}\right\rfloor,\quad l_{12},\cdots,\quad l_{14}\right] \tag{51}$$

The initial population of the following loop is generated by analogy. The flow chart of the optimization method proposed in this paper is illustrated in Fig.5.

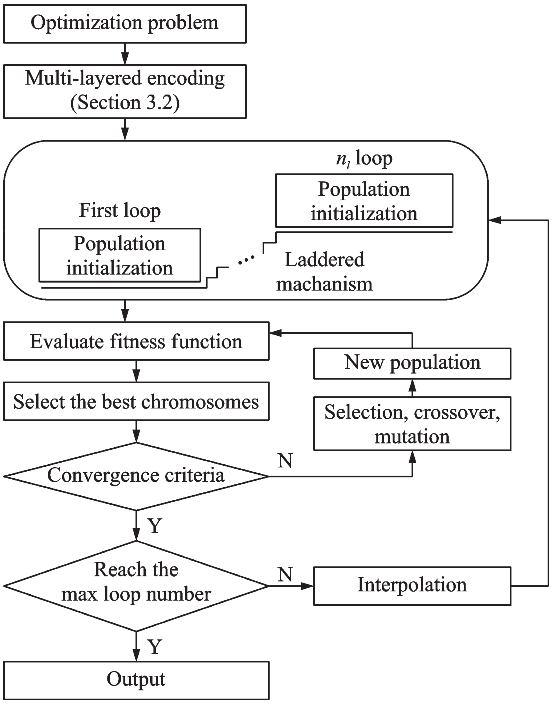

Fig.5 Flow chart of laddered multi-layer GA

Remark 3 Taking advantage of the multilayered coding sequence of candidate positions, the population initialization can be simply formulated using interpolations since the uniform mapping from physical space to numerical coding space.

3 Numerical Simulations

To verify the effectiveness of the proposed methods, including the modeling of the flexible spacecraft and its large flexible antenna, the optimization criteria, and the performance of the optimization algorithm, simulations are carried out. First, an eight-actuator optimized configuration is achieved using the modeling （Section 1） and the optimization scheme （Section 2）. The performance of the optimization algorithm is compared with that used in Ref.[24]. Second， the coupling-reducing performance of the optimized placement is compared with that of the traditional criteria in Ref.[37]， using Monte Carlo simulation in an attitude-vibration stabilizing scenario. Independent attitude and vibration control， linear quadratic regulator （LQR） is adopted to evaluate the performance of the optimal placement result

3.1 Optimizing placement of PSAs

Here， a performance comparison between the GA proposed in this paper and that used in Ref.[24] is presented using three cases. Besides， two different types of actuators layout using traditional optimization criteria and that in this paper are achieved for further use in the next section to show the vibration-attitude coupling effect damping superiority of the proposed method. The GA initialization parameters are shown in Table 3. And parameters used for problem setup are presented in Table 4.

Table 3 GA initialization parameters

Parameter	Case 1： Method in Ref.[24]	Case 2： Combined method in Ref.[24] and the proposed method	Case 3： The proposed method
Initial population	[1 570,1 402, 1 234, 10 628, 5, 897, 7 560, 392]	[1 570, 1 402, 1 234, 1 065, 897, 728, 560, 392]	[1 570, 1 178, 785, 392]
Population size	1 600	120	120
Crossover fraction	0.5	0.5	0.5
Migration fraction	0.9	0.9	0.9
Max generations	16 000	5 000	5 000
Stall gen limit	1 000	1 000	1 000
Function tolerance	1×10^{-8}	1×10^{-8}	1×10^{-8}

Table 4 Properties of honeycomb structure

Parameter	Value
Number of beams	2 438
Number of candidate beams	1 570
Number of actuators	8
Order of modes	10
Number of layers	130
Cross-sectional area/m^2	3.46×10^{-5}
Layer thickness/m	120×10^{-6}
d_{33}/(m•V^{-1})	568×10^{-12}
c_{33}^{E}/Pa	6.75×10^{10}
Max force of PSAs/N	1 000

Table 1 shows the first eight mode frequencies derived from commercial FEM software to establish the mathematical model. The convergence process and outcome are shown in Fig.6 and Table 5. As can be seen from the results， when using the population size of 1 600， the maximum generation size of 16 000 and the exact GA optimization method， which is utilized in Ref.[24] whose optimization target has 1 281 candidate nodes and 6 actuators are considered， it takes 1 056.5 s to converge to a relatively low fitness value of 844 643.5 in case 1. However， when using the combined optimization of this paper and that in Ref.[24]， that is， only the multi-layered coding technique rather than other methods proposed in this paper is utilized， it takes less population of 120 and less time of 380.8 s to achieve a better fitness value 126 660 in case 2. When the proposed method is fully utilized， a better fitness value of 171 846 is achieved using even less time of 206.5 s. Note that all the stopping criteria of these algorithms are set as same （Table 2） and all the tested cases have reached the stopping criteria before ending the optimization process （Fig.6）. The less optimized result of actuators placement obtained by case 1 and case 2 can result in the reduction in active vibration control performance and even in the instability of the system due to the limited maximum of actuators output（in this case is 1 000 N）. However，

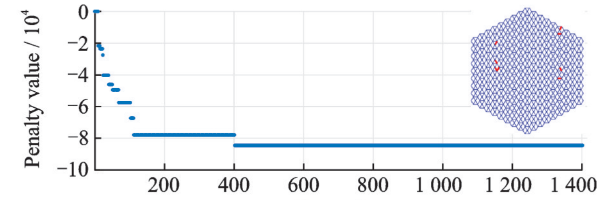

(a) Case 1—best: −84 463.5

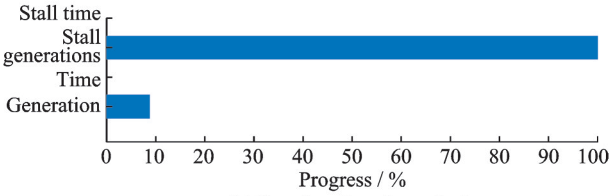

(b) Case 1—Stopping criteria

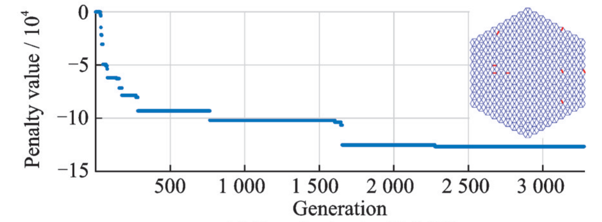

(c) Case 2—best: −126 660

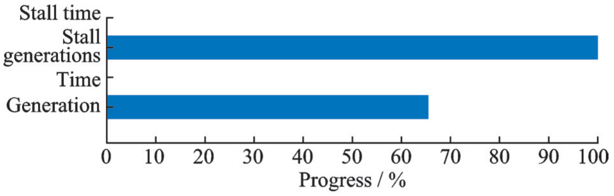

(d) Case 2—Stopping criteria

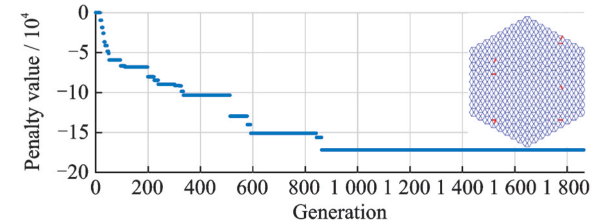

(e) Case 3—best: −171 846

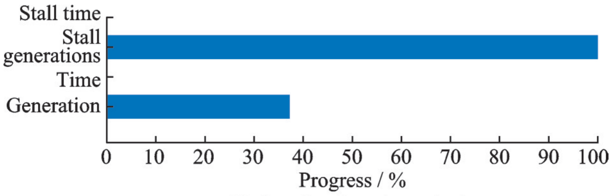

(f) Case 3—Stopping criteria

Fig.6　Convergence procedure of optimization comparison

Table 5　Performance comparison of optimization algorithms

Performance criteria	Case 1	Case 2	Case 3
Best fitness value	84 463.5	126 660	171 846
Generation consumption	1 402	3 276	1 863
Time consumption (@i7-14700)/s	1 056.5	380.8	206.5

since the main concern of this paper is to enhance the coupling-damping characteristic of the actuator layout, this phenomenon is not presented here for simplicity.

The placement result derived from traditional criteria (Eq.(31)) and the proposed criteria (Eq.(48)) both using the optimization algorithm in this paper are shown as placement Type A and Type B in Fig.7. And the corresponding coding number is shown in Table 6. As can be seen from the result, both the optimized placement achieved from traditional criteria and that of this paper show a roughly central symmetric pattern, which is as supposed in former sections. Besides, the results in Refs.[23, 29] also show the symmetric pattern, which adds to the reliability of this paper. By considering the coupling effect reducing objective, the proposed configuration shows a larger average distance from installation place to the origin where the flexible structure is connect to the rigid hub.

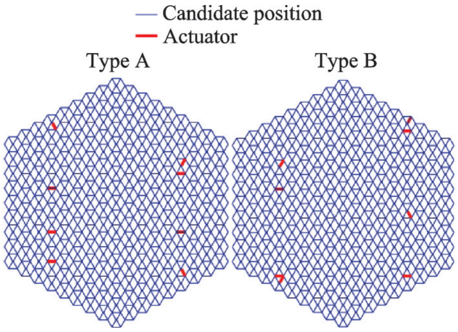

Fig.7　Displacement result comparison

Table 6　Types and their position numbers

Type	Position number
A	[1 468, 1 434, 986, 883, 674, 587, 230, 55]
B	[1 354, 1 343, 997, 816, 560, 551, 150, 55]

3.2　Overall performance evaluation under attitude-vibration stabilization control

An attitude stabilization scenario where the spacecraft is impacted by a high-speed space debris is considered. Two configurations achieved in Section 3.1 are compared in the same scenario. The initial parameters are shown as follow. The initial attitude angle, vibration mode and their derivatives are all 0. The mass property of the spacecraft is set as Table 7. The magnitude of the disturbance torque introduced by the debris is 1 000 N•m, and its direction is decided by the specific Monte Carlo simulation trail. The impact takes place at time instant 50 s, and the duration is 0.01 s. The number of Monte Carlo trails is set as 300 in this case, which produces the impacting torque that has the distribution as in Fig.8.

Table 7 Parameters of the system

Parameter	Value
Rigid hub mass/kg	5 000
Structure mass/kg	2 000
Inertia matrix/ (kg•m^2)	$\begin{bmatrix} 0.6\times10^6 & 0 & 0 \\ 0 & 0.6\times10^6 & 0 \\ 0 & 0 & 0.1\times10^7 \end{bmatrix}$
$\boldsymbol{B}_{\mathrm{tran}}$	Defined in appendix
$\boldsymbol{B}_{\mathrm{rot}}$	Defined in appendix

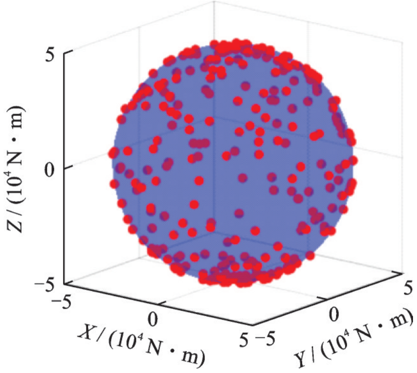

Fig.8 Impact torque distribution of Monte Carlo

Since the main objective of this paper is to compare different PSA placements, both ACS and AVCS are implemented using independent LQR controllers. The controller design is kept standard so that the performance difference comes solely from PSA placement. Based on the coupled dynamics in Eq.(24), the attitude subsystem is linearized as

$$\dot{\boldsymbol{x}}_{\mathrm{a}}=\boldsymbol{A}_{\mathrm{a}}\boldsymbol{x}_{\mathrm{a}}+\boldsymbol{B}_{\mathrm{a}}\boldsymbol{u}_{\mathrm{a}}+\boldsymbol{d}_{\mathrm{a}},\quad \boldsymbol{x}_{\mathrm{a}}=[\boldsymbol{\theta},\boldsymbol{\omega}] \tag{52}$$

The flexible subsystem derived from Eqs.(14—15) is written as

$$\dot{\boldsymbol{x}}_{\mathrm{v}}=\boldsymbol{A}_{\mathrm{v}}\boldsymbol{x}_{\mathrm{v}}+\boldsymbol{B}_{\mathrm{v}}\boldsymbol{u}_{\mathrm{v}}+\boldsymbol{d}_{\mathrm{v}},\quad \boldsymbol{x}_{\mathrm{v}}=[\boldsymbol{\eta}_i,\dot{\boldsymbol{\eta}}_i] \tag{53}$$

For each subsystem, the LQR gain is obtained from its corresponding algebraic Riccati equation.

For ACS, the Riccati equation is

$$\boldsymbol{A}_{\mathrm{a}}^{\mathrm{T}}\boldsymbol{P}_{\mathrm{a}}+\boldsymbol{P}_{\mathrm{a}}\boldsymbol{A}_{\mathrm{a}}-\boldsymbol{P}_{\mathrm{a}}\boldsymbol{B}_{\mathrm{a}}\boldsymbol{R}_{\mathrm{a}}^{-1}\boldsymbol{B}_{\mathrm{a}}^{\mathrm{T}}\boldsymbol{P}_{\mathrm{a}}+\boldsymbol{Q}_{\mathrm{a}}=0 \tag{54}$$

and the feedback gain is

$$\boldsymbol{K}_{\mathrm{a}}=\boldsymbol{R}_{\mathrm{a}}^{-1}\boldsymbol{B}_{\mathrm{a}}^{\mathrm{T}}\boldsymbol{P}_{\mathrm{a}} \tag{55}$$

For AVCS, the Riccati equation is

$$\boldsymbol{A}_{\mathrm{v}}^{\mathrm{T}}\boldsymbol{P}_{\mathrm{v}}+\boldsymbol{P}_{\mathrm{v}}\boldsymbol{A}_{\mathrm{v}}-\boldsymbol{P}_{\mathrm{v}}\boldsymbol{B}_{\mathrm{v}}\boldsymbol{R}_{\mathrm{v}}^{-1}\boldsymbol{B}_{\mathrm{v}}^{\mathrm{T}}\boldsymbol{P}_{\mathrm{v}}+\boldsymbol{Q}_{\mathrm{v}}=0 \tag{56}$$

and the feedback gain is

$$\boldsymbol{K}_{\mathrm{v}}=\boldsymbol{R}_{\mathrm{v}}^{-1}\boldsymbol{B}_{\mathrm{v}}^{\mathrm{T}}\boldsymbol{P}_{\mathrm{v}} \tag{57}$$

The ACS uses identical gains for all three rotational axes, and all vibration modes share the same set of modal gains. The numerical values employed in simulation are listed in Table 8. It is noted that those numerical values are the LQR weight matrices ($\boldsymbol{Q}_{\mathrm{a}},\boldsymbol{R}_{\mathrm{a}}$) and ($\boldsymbol{Q}_{\mathrm{v}},\boldsymbol{R}_{\mathrm{v}}$). The final feedback gains used in the simulations, $\boldsymbol{K}_{\mathrm{a}}$ and $\boldsymbol{K}_{\mathrm{v}}$, are obtained from these weights via the standard LQR solution $\boldsymbol{K}=\boldsymbol{R}^{-1}\boldsymbol{B}^{\mathrm{T}}\boldsymbol{P}$, where $\boldsymbol{P}$ is the solution of the algebraic Riccati equation. Thus, specifying ($\boldsymbol{Q},\boldsymbol{R}$) fully determines ($\boldsymbol{K}_{\mathrm{a}},\boldsymbol{K}_{\mathrm{v}}$), and both descriptions are equivalent.

Table 8 Parameters of controller

System	Parameter	Value
ACS	$\boldsymbol{Q}_{\mathrm{a}}$	diag(1 400, 4 × 10^4)
	$\boldsymbol{R}_{\mathrm{a}}$	$\boldsymbol{I}$
AVCS	$\boldsymbol{Q}_{\mathrm{v}}$	diag(0.1, 0. 1)
	$\boldsymbol{R}_{\mathrm{v}}$	$\boldsymbol{I}$

To evaluate the capability of the proposed method to reduce pose-vibrational coupling effect, the energy consumption of the reaction wheel during the attitude stabilization period is defined as

$$E_{\mathrm{a}}=\int_{t_0}^{T_{\mathrm{f}}}(|T_x|+|T_y|+|T_z|)\,\mathrm{d}t \tag{58}$$

Similar to the energy consumption evaluation, the maximum Euler angle magnitude excited by the vibration control is defined as

$$M_{\mathrm{A}}=\max(|\Delta\psi|)+\max(|\Delta\theta|)+\max(|\Delta\varphi|) \tag{59}$$

where $\Delta\psi$, $\Delta\theta$ and $\Delta\varphi$ are the attitude errors compared to rigid body dynamics. For convenience, the unordered result of Monte Carlo simulation is sorted in a descending way of the energy consumption of Type A configuration.

According to Fig.9, the ACS consumption of the PSA configuration Type B shows its advantage even when disturbance torque in all directions is considered. It saves up to 15% of energy, compared with Type A. And the percentage of its saving descends as the total consumption descends. According to Fig.10, the excited attitude error shows up to 6% of reduction, with maximum magnitude of 0.1°. This advantage is notable for missions that have strict requirement on pointing accuracy.

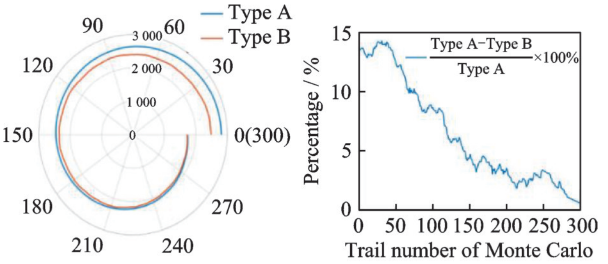

(a) ACS energy consumption (b) ACS energy consumption reduction percentage

Fig.9 ACS energy consumption reduction percent

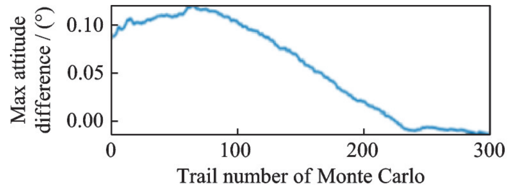

(a) Max attitude difference of Type A and Type B

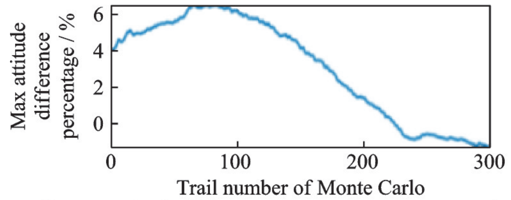

(b) Max attitude difference percentage of Type A and Type B

Fig.10 Max attitude difference in Monte Carlo simulation

3.3 Case study under attitude-vibration stabilization control

A slice of the Monte Carlo simulation is presented here to help demonstrate the effectiveness of the proposed method. In this case the disturbance torque is along the yaw axis. All the other parameters are exactly the same as those in Section 3.2.

As shown in Figs.11, 12, the impact disturbance from the debris and the coupling disturbance from the active vibration control system occur simultaneously at 50 s. However, due to the varying degrees of coupling effects induced by different placements of the PSAs, the excited attitude Euler angles exhibit significant variation.

In Figs.11—13, the results show that the criteria proposed in this paper can reduce the attitude-vibration coupling effect by over 10%, along with an over 10% reduction in the flywheel energy consumption and nearly 50% reduction in settling time of the probe displacement. Note that the stabilized state of the vibration control is defined as the tip displacement of 12 probes are less than 1 mm.

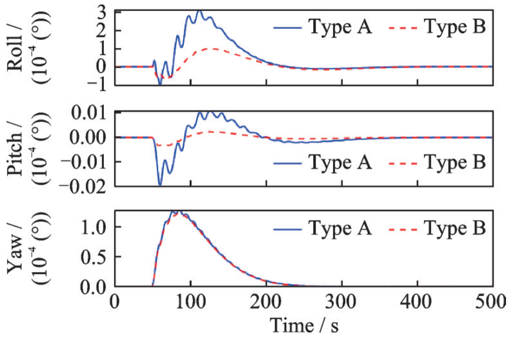

Fig.11 Attitude responses during stabilization control

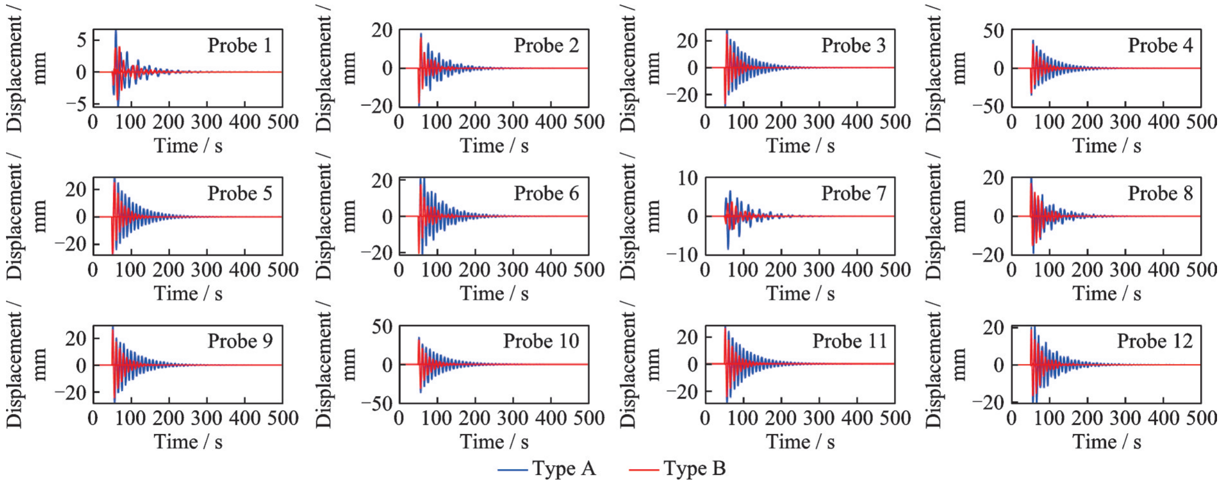

Fig.12 Displacement responses of 12 probes

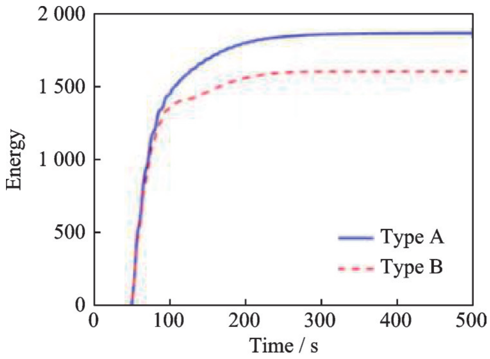

(a) Energe consumption of reaction wheel

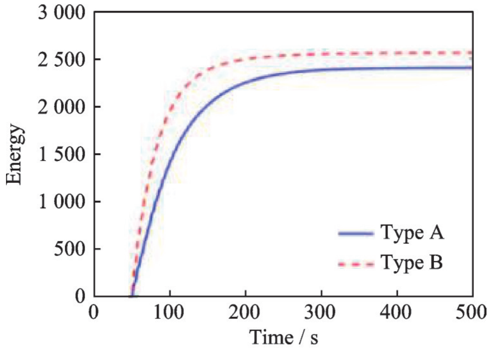

(b) Energy consumption of PSA

Fig.13 Energy consumptions of reaction wheel and PSA

The only compromise is the energy consumption of PSA, which suffers 10% additional increase. However, this pitfall is tolerable compared with its advantages, especially for LSS whose pointing accuracy and stabilizing settling time are the main concerns of its mission.

In Fig.14(a) , the debris impacting torque of 5 000 N·m at 50 s leads to an approximately 2 500 N·m coupling torque at the commence. After the impact, the attitude-vibration coupling torque of Type B placement is dramatically lower than that of Type A, which shows the coupling-reduced functionality of optimal criteria proposed in Section 2.3. Meanwhile, Fig.14(b) shows that, since the translation coupling matrix $\boldsymbol{B}_{\text{tran}}$ is also considered in Eq.(44), although with a smaller weighting coefficient $\boldsymbol{H}_{\text{tran}}$ compared with $\boldsymbol{H}_{\text{rot}}$, the flexible-rigid coupling force generated by Type B configuration is also slightly less than that by the traditional Type A method. Fig.15 shows that the oscillation of intended control torque of reaction wheel under Type B configuration is also obviously less than that of Type A, which benefits the application in practice.

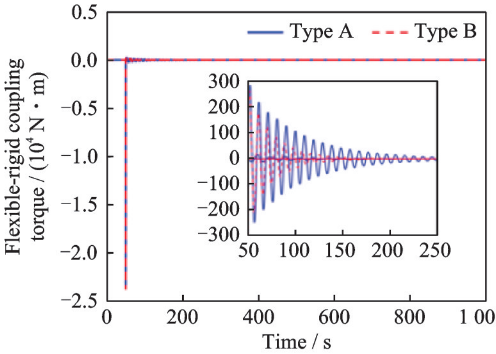

(a) Flexible-rigid coupling torque of Type A and Type B

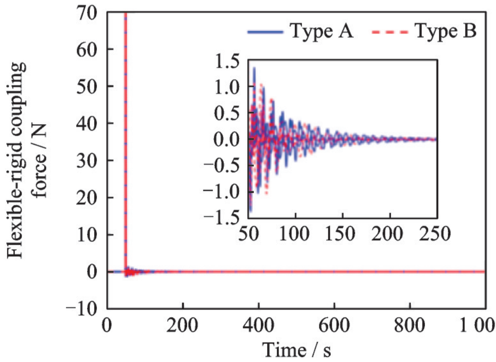

(b) Flexible-rigid coupling force of Type A and Type B

Fig.14 Attitude responses during stabilization control

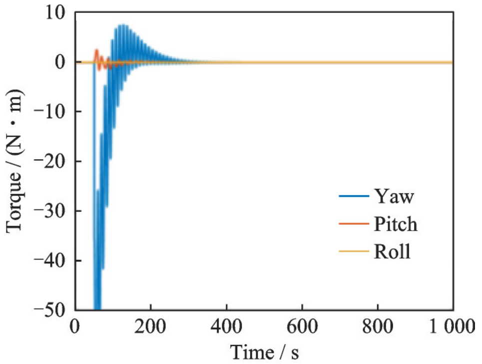

(a) Reaction wheel torque of Type A

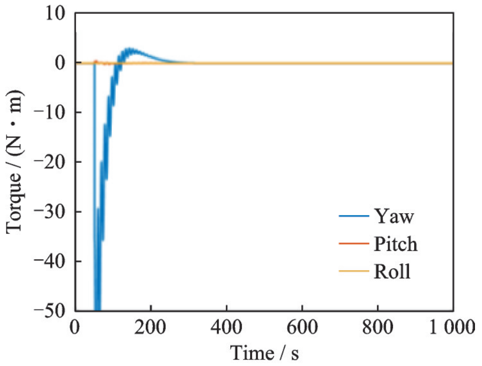

(b) Reaction wheel torque of Type B

Fig.15 Attitude control inputs under debris impact

4 Conclusions

This study designs a spacecraft with a large telescope structure that can fit into a high resolution exoplanet observing mission, followed by a design scheme of coupling-reduced optimal actuator placement for the large flexible honeycomb shaped telescope structure. Unlike existing methods, an attitude-vibration coupling effect damping criteria for the optimal placement of PSA is proposed. A laddered multilayer GA algorithm is designed to solve the gigantic discrete optimization problem numerically. According to the results, the proposed method shows its effectiveness in reducing the coupling effect between AVCS and ACS of the spacecraft in terms of less attitude control effort, less excited attitude error, and less convergence time of the vibration and attitude control system.

This paper further shows that the optimal placement of vibration actuators plays an important role in improving the control system performance of flexible spacecraft with large space structures. And the difficulties of optimization caused by the increasing size and complexity of large space structures should be well handled.

Our future work will extend the proposed placement framework to nonlinear and parameter-varying models, including thermo-elastic effects and large-angle maneuvers, to further assess robustness in practical mission scenarios.

Appendix Coupling Matrix of Spacecraft

The coupling matrices calculated from Eq.(27) are listed here.

$$\boldsymbol{B}_{\mathrm{rot}}^{\mathrm{T}}=\begin{bmatrix} -11.6536 & -770.1883 & -5.5483\times 10^{-5} \\ -0.9057 & 0.2361 & 0.8721 \\ -765.3492 & -0.0053 & 0.0243 \\ 0.6986 & 0.1191 & -0.7424 \\ 0.0910 & 0.0177 & 89.1661 \\ -0.1097 & -0.0014 & 1079.7489 \\ 13.5040 & 125.1317 & 0.0107 \\ -69.3869 & 0.0078 & -0.0497 \\ -0.8604 & -0.3211 & 0.3539 \\ -1.3824 & 0.0063 & -57.1871 \end{bmatrix}$$

$$\boldsymbol{B}_{\mathrm{tran}}^{\mathrm{T}}=\begin{bmatrix} -3.445 & 1.059\times 10^{-10} & -2.389\times 10^{-10} \\ 2.042\times 10^{-9} & -1.753\times 10^{-9} & 4.098\times 10^{1} \\ -1.975\times 10^{-8} & 1.708 & 8.128\times 10^{-10} \\ 1.088\times 10^{-10} & 4.005\times 10^{-11} & 3.383\times 10^{1} \\ 4.987\times 10^{-11} & -1.612\times 10^{-11} & -7.801\times 10^{-11} \\ 2.011\times 10^{-10} & 6.476\times 10^{-11} & 9.022\times 10^{-11} \\ -2.612 & 5.435 & -7.801\times 10^{-11} \\ 1.644\times 10^{-11} & -3.946\times 10^{-10} & -9.784 \\ 1.999\times 10^{-10} & -9.188\times 10^{-11} & -5.549\times 10^{-11} \\ -1.360\times 10^{-10} & 8.791\times 10^{-12} & -1.569\times 10^{-10} \end{bmatrix}$$

References

[1] CHANG B Y, GUAN X, LIANG D, et al. Design and dynamic analysis of supporting mechanism for large scale space deployable membrane sunshield[J]. The Aeronautical Journal, 2024, 128(1327): 1974-2002.

[2] XUE Z H, LIU J G, WU C C, et al. Review of in-space assembly technologies[J]. Chinese Journal of Aeronautics, 2021, 34(11): 21-47.

[3] LIU Z Q, QIU H, LI X, et al. Review of large spacecraft deployable membrane antenna structures[J]. Chinese Journal of Mechanical Engineering, 2017, 30(6): 1447-1459.

[4] SABATINI M, GASBARRI P, MONTI R, et al. Vibration control of a flexible space manipulator during on orbit operations[J]. Acta Astronautica, 2012, 73: 109-121.

[5] HUANG Z R, TANG C, YU Q, et al. Dynamics and FNTSM control of spacecraft with a film capture pocket system[J]. Space: Science & Technology, 2023, 3: 79.

[6] CAO Y T, CAO D Q, HE G Q, et al. Thermal alternation induced vibration analysis of spacecraft with lateral solar arrays in orbit[J]. Applied Mathematical Modelling, 2020, 86: 166-184.

[7] SHANNON R. Numerical study of hypervelocity space debris impacts on CFRP/Al honeycomb spacecraft structures[C]//Proceedings of the 55th International Astronautical Congress of the International Astronautical Federation, the International Academy of Astronautics, and the International Institute of Space Law. Vancouver, Canada: AIAA, 2004.

[8] MENG D S, LIU H D, LI Y N, et al. Vibration suppression of a large flexible spacecraft for on-orbit operation[J]. Science China Information Sciences, 2017, 60(5): 050203.

[9] ZHAO X N, ZHANG S, LIU Z J, et al. Vibration control for flexible manipulators with event-triggering mechanism and actuator failures[J]. IEEE Transactions on Cybernetics, 2022, 52(8): 7591-7601.

[10] DI GENNARO S. Passive attitude control of flexible spacecraft from quaternion measurements[J]. Journal of Optimization Theory and Applications, 2003, 116(1): 41-60.

[11] CHEN T, WANG Y K, WEN H, et al. Autonomous assembly of multiple flexible spacecraft using RRT* algorithm and input shaping technique[J]. Nonlinear Dynamics, 2023, 111(12): 11223-11241.

[12] XU S J, CUI N G, FAN Y H, et al. Active vibration

suppression of flexible spacecraft during attitude maneuver with actuator dynamics[J]. IEEE Access, 2018, 6: 35327-35337.

[13] GUAN Ping, HUANG Mingliang, GE Xinsheng, et al. Fuzzy model predictive control of large flexible spacecraft[J]. Aerospace Control, 2023, 41(3): 43-49. (in Chinese)

[14] TAYEBI J, CHEN T, WANG H. Dynamics and control of flexible satellite using reaction sphere actuators[J]. Space: Science & Technology, 2023, 3: 77.

[15] ZHU X Y, ZHU Z H, CHEN J L. Dual quaternion-based adaptive iterative learning control for flexible spacecraft rendezvous[J]. Acta Astronautica, 2021, 189: 99-118.

[16] MENG B, ZHAO Y B. The dynamics characteristics of flexible spacecraft and its closed-loop stability with passive control[J]. Journal of Systems Science and Complexity, 2021, 34(3): 860-872.

[17] HU Q L. Robust adaptive sliding mode attitude maneuvering and vibration damping of three-axis-stabilized flexible spacecraft with actuator saturation limits[J]. Nonlinear Dynamics, 2009, 55(4): 301-321.

[18] HU Q L, MA G F. Variable structure control and active vibration suppression of flexible spacecraft during attitude maneuver[J]. Aerospace Science and Technology, 2005, 9(4): 307-317.

[19] SABATINI M, PALMERINI G B, GASBARRI P. Synergetic approach in attitude control of very flexible satellites by means of thrusters and PZT devices[J]. Aerospace Science and Technology, 2020, 96: 105541.

[20] HU Y B, GENG Y H, WU B L. Flexible spacecraft vibration suppression by distributed actuators[J]. Journal of Guidance, Control, and Dynamics, 2020, 43(11): 2141-2147.

[21] LU E, LI W, YANG X F, et al. Optimal placement and active vibration control for piezoelectric smart flexible manipulators using modal H_2 norm[J]. Journal of Intelligent Material Systems and Structures, 2018, 29(11): 2333-2343.

[22] ABUALRUB T, ABUKHALED M, JAMAL B. Wavelets approach for the optimal control of vibrating plates by piezoelectric patches[J]. Journal of Vibration and Control, 2018, 24(6): 1101-1108.

[23] GUO J Y, YUE C F, JIA S Y, et al. Plate-like flexible spacecraft modeling and distribution of control moment gyroscopes[J]. Space: Science & Technology, 2023, 3: 68.

[24] JIA S Y, SHAN J J. Optimal actuator placement for constrained gyroelastic beam considering control spillover[J]. Journal of Guidance, Control, and Dynamics, 2018, 41(9): 2073-2081.

[25] LI W G, YANG Z C, LI K, et al. Hybrid feedback PID-FxLMS algorithm for active vibration control of cantilever beam with piezoelectric stack actuator[J]. Journal of Sound and Vibration, 2021, 509: 116243.

[26] SHIVASHANKAR P, GOPALAKRISHNAN S. Review on the use of piezoelectric materials for active vibration, noise, and flow control[J]. Smart Materials and Structures, 2020, 29(5): 053001.

[27] LI W P, HUANG H. Integrated optimization of actuator placement and vibration control for piezoelectric adaptive trusses[J]. Journal of Sound and Vibration, 2013, 332(1): 17-32.

[28] KOUIDER B, POLAT A. Optimal position of piezoelectric actuators for active vibration reduction of beams[J]. Applied Mathematics and Nonlinear Sciences, 2020, 5(1): 385-392.

[29] ANGELETTI F, GASBARRI P, SABATINI M, et al. Design and performance assessment of a distributed vibration suppression system of a large flexible antenna during attitude manoeuvres[J]. Acta Astronautica, 2020, 176: 542-557.

[30] QI Y F, SHAN M H. Simulation on flexible multibody system with topology changes for in-space assembly[J]. The Journal of the Astronautical Sciences, 2024, 71(2): 11.

[31] BRECKINRIDGE J B, HARVEY J, IRVIN R G, et al. Stealth telescopes for space and ground astronomy[C]//Proceedings of UV/Optical/IR Space Telescopes and Instruments: Innovative Technologies and Concepts Ⅸ. San Diego, USA: SPIE, 2019: 17.

[32] YANG Yidai, JING Wuxing, ZHANG Zhao. A new method for orbit and attitude coupling control problem of flexible spacecraft based on dual quaternions[J]. Journal of Astronautics, 2016, 37(8): 946-956. (in Chinese)

[33] DING Z M, WANG C J, WU H Y, et al. Dynamic analysis of modular space deployable supporting structure[C]//Proceedings of the 2018 10th International Conference on Measuring Technology and Mechatronics Automation (ICMTMA). Changsha, China: IEEE, 2018: 337-340.

[34] KHOT N S, VENKAYYA V B, EASTEP F E. Optimal structural modifications to enhance the active vibration control of flexible structures[J]. AIAA Journal, 1986, 24(8): 1368-1374.

[35] ANGELETTI F, IANNELLI P, GASBARRI P, et

al. End-to-end design of a robust attitude control and vibration suppression system for large space smart structures[J]. Acta Astronautica, 2021, 187: 416-428.

[36] MAIN J A, GARCIA E. Piezoelectric stack actuators and control system design: Strategies and pitfalls[J]. Journal of Guidance, Control, and Dynamics, 1997, 20(3): 479-485.

[37] LELEU S, ABOU-KANDIL H, BONNASSIEUX Y. Actuators and sensors positioning for active vibration control in flexible systems[J]. IFAC Proceedings Volumes, 2000, 33(26): 935-940.

Acknowledgement This work was supported by National Natural Science Foundation of China (No.U23B6001).

Authors

The first author Prof. **GUO Yanning** received his M.S. and Ph.D. degrees in control science and engineering from Harbin Institute of Technology, Harbin, China, in 2008 and 2012, respectively. He is currently a professor with Department of Control Science and Engineering, Harbin Institute of Technology, and performs research in the fields of deep space exploration, satellite attitude control, and nonlinear control.

The corresponding author Dr. **RAN Guangtao** received his Ph.D. degree in control science and engineering from Harbin Institute of Technology, Harbin, China in 2023. From 2021 to 2022, he was a joint Ph.D. candidate with Department of Electrical and Computer Engineering, University of Alberta, Edmonton, Canada. He is currently an assistant professor with Department of Control Science and Engineering, Harbin Institute of Technology, China. His current research interests include multi-agent systems, optimal control, fuzzy control, fault detection, networked control systems, and security control.

Author contributions Prof. **GUO Yanning** designed the study, compiled the models, conducted the analysis, interpreted the results, and wrote the manuscript. Mr. **DENG Yuchen** contributed to data and model components for the model. Dr. **RAN Guangtao** revised the manuscript and contributed to the numerical simulation. Prof. **LIU Fucheng** contributed to the discussion and background of the study. All authors commented on the manuscript draft and approved the submission.

Competing interests The authors declare no competing interests.

(Production Editor: WANG Jie)

柔性望远镜航天器压电作动器降耦合最优布局优化

郭延宁[1,2]，邓宇辰[1]，冉光滔[1]，刘付成[3]

(1.哈尔滨工业大学航天学院,哈尔滨 150001,中国; 2.哈尔滨工业大学郑州高等研究院,郑州 450000,中国;
3.上海交通大学航空航天学院,上海 200240, 中国)

摘要:大型空间结构(Large space structure, LSS)通常具有低固有频率特征,易在轨激励下产生振动振荡。随着柔性结构尺度增大,结构振动控制与航天器姿态控制之间的耦合效应将显著削弱整体控制性能。为此,提出一种用于压电叠堆作动器(Piezoelectric stack actuators, PSAs)网络的最优布局方法,以降低姿态-振动控制系统间的耦合影响。首先,面向分辨率敏感的成像任务,设计了一种蜂窝形柔性望远镜航天器结构,并基于有限元模型(Finite element method, FEM)与浮动参考系方法(Floating frame of reference formulation, FFRF)建立其耦合动力学模型。随后,构造了一种融合耦合矩阵的增强Gramian优化准则,在抑制耦合激励的同时兼顾系统可控性。进一步地,提出一种阶梯式多层优化框架,以提升求解超大规模离散优化问题的效率与精度。最后,通过数值仿真验证了所提方法在降低耦合效应与提升控制性能方面的有效性。

关键词:大型空间结构;挠性航天器控制;作动器布局优化;振动控制;刚柔耦合航天器